Cobalt and Iron Phosphates with Modulated Compositions and Phases as Efficient Electrocatalysts for Alkaline Seawater Oxidation

Chandni Das[a,b] and Poulomi Roy[a,b]*

[a]Materials Processing & Microsystems Laboratory, CSIR – Central Mechanical Engineering Research Institute (CMERI), Mahatma Gandhi Avenue, Durgapur 713209, West Bengal, India.

[b]Academy of Scientific and Innovative Research (AcSIR), Ghaziabad - 201 002, India.

*Email: poulomiroy@yahoo.com, p.roy@cmeri.res.in

Experimental Section

Material synthesis

All the chemicals used in the experiments were without any purification. The pristine cobalt phosphate, iron phosphate and mixed metal phosphates were synthesized by a simple single step solvothermal treatment. $CoCl_2.6H_2O$ (Merck, ≥ 98%), anhydrous $FeCl_3$ (Merck, ≥ 98%) and $NaH_2PO_4.H_2O$ (Merck, ≥ 99%) were used as metal precursors and phosphate precursor, respectively.

A total 10 mM of metal precursors and 20 mM of phosphate precursor were dissolved in a solvent mixture of isopropyl alcohol and ultrapure deionized water in 2:1 ratio to obtain a homogenous solution which was then transferred into 40 ml Teflon-lined stainless steel autoclave and was maintained at 140°C for 14 h in a hot air oven. After the completion of the reaction, the autoclave was naturally cooled down to room temperature. The obtained products were filtered and washed several times with DI water and finally with ethanol. The collected samples were then dried overnight under vacuum. The variation of metal precursor concentrations in pristine and mixed metal phosphates are stated in Table S1 and named accordingly.

Table S1. Reaction parameters for the synthesis of pristine metal phosphates and mixed metal phosphates.

Sample Code	Reaction condition	Co-precursor	Fe-precursor	P-precursor
C10F0	140 ºC / 14 h	10 mM	0 mM	20 mM
C7F3		7 mM	3 mM	
C5F5		5 mM	5 mM	
C3F7		3 mM	7 mM	
C0F10		0 mM	10 mM	

Structural characterisation

The powder X-ray diffraction (XRD) patterns of the materials were evaluated to obtain the composition and phase purity using Rigaku Miniflex-600 in the 2θ range of 8°─80° using Cu K∞ radiation (λ = 1.5418 Å). The morphology of the samples were characterized by field emission scanning electron microscopy (FE-SEM, Carl Zeiss, Germany) at 5 kV. Transmission electron microscopy (TEM) studies were carried out on a JEM-3200FS Electron Microscope is equipped with a field emission electron gun of 300 kV accelerating voltage. The samples were prepared by taking a drop of dispersed sample in ethanol on a carbon-coated copper grid. The elemental states of the samples were carried out by X-ray photoelectron spectroscopy (XPS) measurement on SCIENTA, R-3000 analyzer with monochromatic Al Kα radiation regarding 1.486 KeV energy maintaining the vacuum of 1 × 10^{-10} Torr. The binding energy of the materials were calibrated with reference to C1s peak near to 284.6 eV and spectrum were collected considering the elements Co, Fe, P and O. Fourier transform infrared spectroscopy (FTIR) of the sample was performed by (IR Prestige-21, SHIMADZU) with an ATR spectrum ranges from 400 cm^{-1} to 4000 cm^{-1}.

Electrochemical measurements

All the electrochemical reactions were carried out at room temperature with Metrohm AutoLab204 using the saturated Ag/AgCl as reference electrode, Pt wire as a counter electrode and the sample as the working electrode in a three-electrode arrangement using 1 M KOH as electrolyte. The working electrodes were prepared by drop casting the obtained sample on Ni foam (2 x 1 cm^2) as substrate. Prior to drop casting, the Ni foams (NFs) were treated with 1 M HCl to remove the native oxide layer under ultrasonication and cleaned with deionized water and ethanol and finally dried. The sample inks were prepared by homogeneous mixing of 2 mg powder sample into 900 μl solution mixture of water and isopropanol in 2:1 ratio and 100 μl PVDF solution under sonication. The series of working electrodes were developed by drop casting sample inks on pre-treated NFs with mass loading of 0.9–1.1 mg cm^{-2}. For comparative study, the conventional RuO_2 electrode was prepared by similar method with mass loading of 1 mg cm^{-2}. The linear sweep voltammetry (LSV) of the electrocatalyst in a three-electrode system were performed sweeping the potential from 0 to 0.8 V with respect to reference saturated Ag/AgCl electrode at sweep rate 5 mV/s. The potential scales of the three electrode system with respect to reversible hydrogen electrode were converted by the equation that is given below:

$$E_{RHE} = E_{appl.} + E_{Ag/AgCl} + 0.059 \times pH \tag{1}$$

To avoid the uncompensated resistance of the circuit, polarization curves were plotted with 100% *iR* correction by following the given equation:

$$E_{iR} = E_{RHE} - iR \tag{2}$$

Where, R is the series resistance (R_s) of the electrochemical circuit, which is the starting point of the impedance along real X-axis in the EIS spectrum for all the prepared series of samples. The obtained series resistance (R_s) value was used to calculate 100% *iR* correction by using eq. (2). Electrochemical impedance spectroscopy (EIS) was analyzed in the frequency range 100 kHz to 0.01Hz with AC potential at 260 mV overpotential of 10 mV magnitude. Chronoamperometry studies of electrocatalysts were measured without *iR* correction. The electrochemical surface area (ECSA) of electrocatalysts were obtained from double layer capacitance (C_{dl}) values in non-faradic region of cyclic voltammetry (CV) obtained at different scan rates following eq. (3):

$$ECSA = \frac{C_{dl}}{C_s} \tag{3}$$

Where, C_{dl} and C_s represent the double layer capacitance and specific capacitance.

Determination turn over frequency (TOF):

The number of active sites were calculated by the cyclic voltammetry (CV) method. All CV measurements were conducted in the potential range of 0 – 0.6 V vs. RHE at a fixed scan rate of 20 mV s^{-1} in 1 M KOH electrolyte with pH = 14.

The TOF value was calculated using the following formula:

$$TOF(s^{-1}) = (j \times A)/(4 \times F \times n) \tag{4}$$

where j (A cm^{-2}) is the current density at a given overpotential, A = 0.75 cm^2 is the geometric surface area of the electrode, F = 96485 C mol^{-1} stands for the Faraday constant, n (mol) = number of active sites.

To further quantitatively probe into the superiority of the as-prepared sample of C7F3 as an electrocatalyst towards the selective OER, its catalytic activity was examined in alkaline sea water (1 M KOH in Sea water) with pH~13.8 obtained from the coastal area of Digha sea beach, West Bengal, India (21.62594^o N, 87.50344^o E). Electrochemical reactions were also performed in a series of alkaline simulated seawater electrolytes of 1.0 M KOH + 1.0 M NaCl, 1.0 M KOH + 0.5 M NaCl and 0.5 M KOH + 0.5 M NaCl and 1.0 M KOH +

seawater. The linear sweep voltammetry (LSV) for OER of the electrocatalyst C7F3 in a three-electrode system were performed sweeping the potential from 0 to 0.8 V with respect to reference saturated Ag/AgCl electrode at sweep rate 5 mV/s. The chronoamperometry analysis was also performed on steady applied potential in 1.0 M KOH + seawater solution to investigate durability of the optimized catalyst.

To evaluate the real ability of the developed electrocatalyst, especially in seawater, the faradaic efficiency of C7F3 has been determined using completely sealed H-cell system with a gas separator membrane in between using alkaline real seawater (1 M KOH + Seawater) as electrolyte. The chronoamperometric (CA) study of C7F3 catalyst was analysed in three electrode system applying 1.67 V vs RHE for 5 min and reaching a current of 0.13 A. Experimentally the evolved O_2 was determined using an oxygen sensor and theoretically the number of moles of oxygen (O_2) produced at anode can be determined from Faraday's second law as given below:

$$n_{theoretical}(O_2) = \frac{Q}{nF} = \frac{I \times t}{nF} \qquad (5)$$

Where, I (A) is the reaching current at applied potential, t (sec) is the duration, n (4) is the number of electrons involved during OER and F (96485 s A mol^{-1}) is Faraday constant. Finally, the faradaic efficiency (*FE*) of the catalyst can be determined as following equation:

$$\text{Faradaic efficiency } (FE) = \frac{n_{O_2}(experimental)}{n_{O_2}(theoretical)} \times 100 = 94.99\% \qquad (6)$$

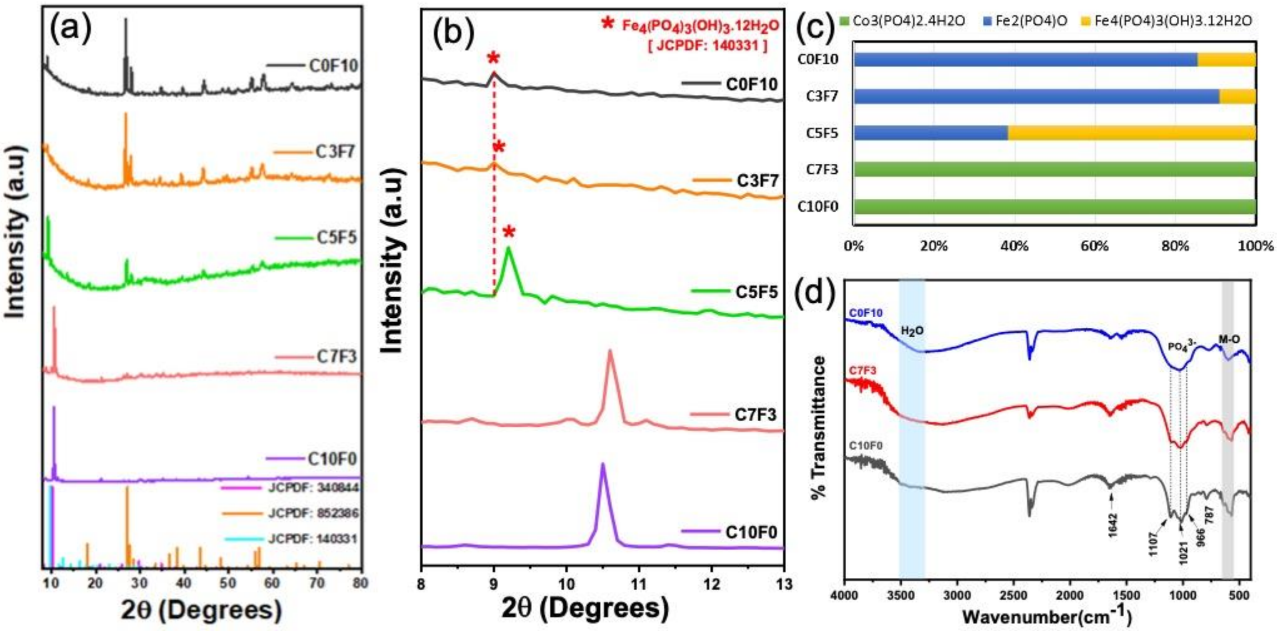

Figure S1: (a) X-ray Diffraction pattern of developed Co and Fe based phosphate samples. (b) Magnified view of the major peak in the entire series showcasing the peak shifting and also the co-existence of phases in C0F10. (c) 100% stacked bar diagram showing the presence of various phases in samples. (d) Fourier transform infra-red spectroscopy analysis of samples.

The FTIR spectroscopy analysis of the synthesized samples has been carried out, as shown in Figure S1(d), to evaluate the molecular groups present in the materials and their corresponding vibrational nature. The characteristic peaks at 966 cm^{-1} can be assigned to symmetric stretching vibrations of P–O bond and peaks at 1021 cm^{-1} and 1107 cm^{-1} to asymmetric stretching vibrations of P–O.[S1] Further, the peak at 787 cm^{-1} confirms the P-O-P linkage present in developed TMPis. The characteristic band in the range of 560-650 cm^{-1} can be attributed to the presence of Co-O and Fe-O bonds in respective TMPis.[S2] The broad peak at around 3400 cm^{-1} and a peak at 1642 cm^{-1} can be assigned to the O–H stretching and bending modes of vibration of water.

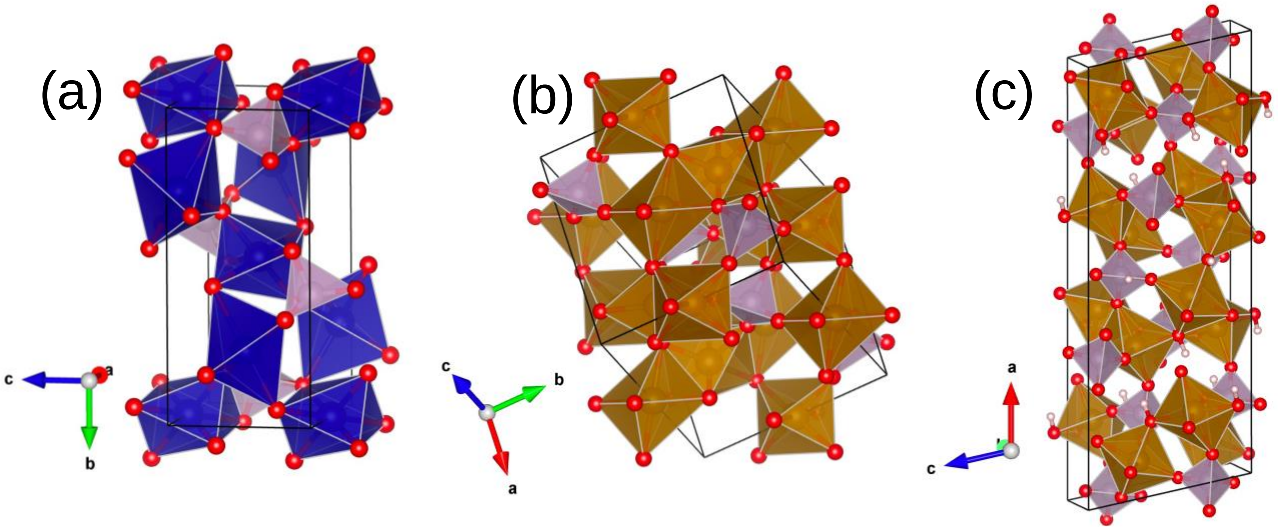

Figure S2: Crystal structures of (a) $Co_3(PO_4)_2$, (b) $Fe_2(PO_4)O$ and (c) $Fe_4(PO_4)_3(OH)_3$.

In $Fe_2(PO_4)O$, iron exists in Fe^{2+} as well as Fe^{3+} and the corresponding crystal structure indicates face sharing octahedra occupied by Fe^{2+} and Fe^{3+}, which allow intervalence charge transfer, which might be beneficial towards OER activity.[S3] Whereas in $Fe_4(PO_4)_3(OH)_3$ and $Co_3(PO_4)_2$, respective Fe^{3+} and Co^{2+} octahedra are separated and linked through phosphate tetrahedra. Such an arrangement in these both phosphates make them not active enough towards OER mechanism as evident from the activities observed by C10F0 containing $Co_3(PO_4)_2$ only and C5F5 composed of $Fe_4(PO_4)_3(OH)_3$ as major phase.

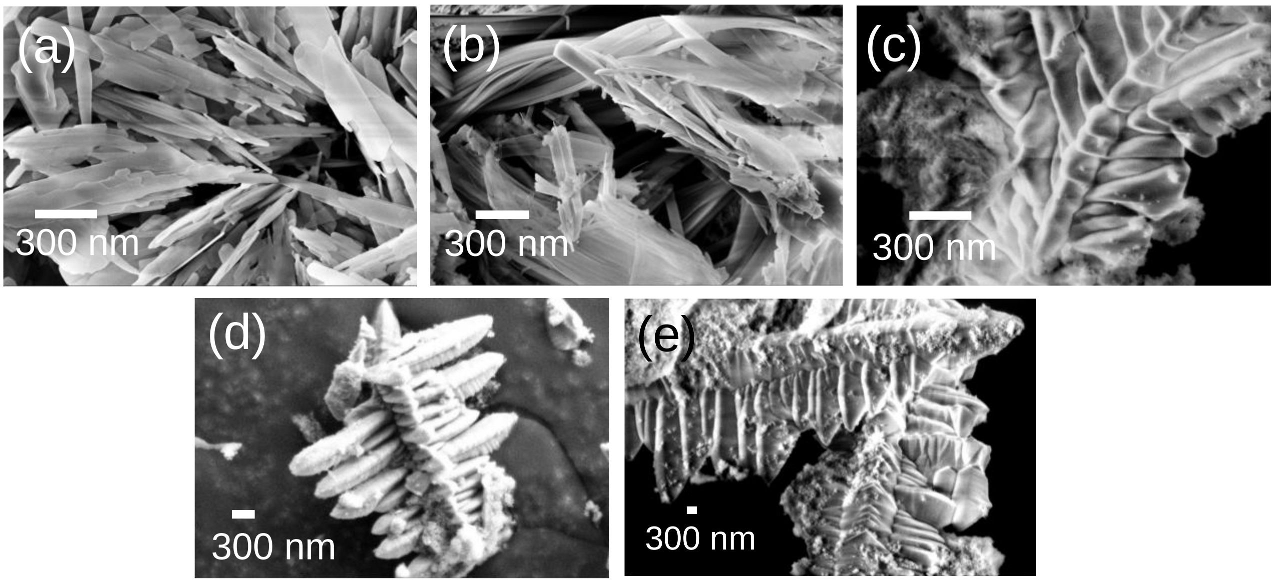

Figure S3. FESEM images of (a) C10F0 (b) C7F3 (c) C5F5 (d) C3F7 (e) C0F10.

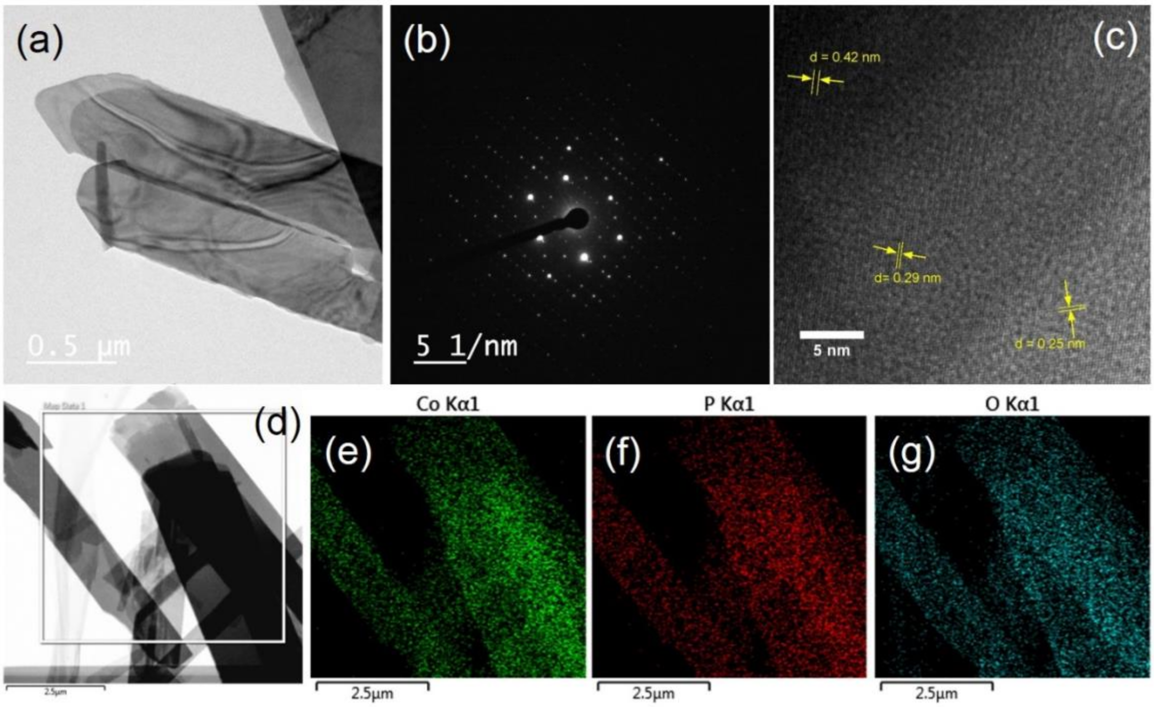

Figure S4. (a)TEM image (b)SAED pattern (c) HRTEM image with d-spacing of C10F0 (d-g) STEM and elemental mapping of Co , P and O in C10F0.

The TEM analysis of C10F0 shows the presence of microrods of dia 400-800 nm. The corresponding SAED pattern suggests the crystalline nature of material and the HRTEM analysis shows the lattice fringes with the spacings of 0.25, 0.29 and 0.42 nm in line with its XRD pattern. The elemental mapping shows homogeneous distribution of all elements throughout the microrods.

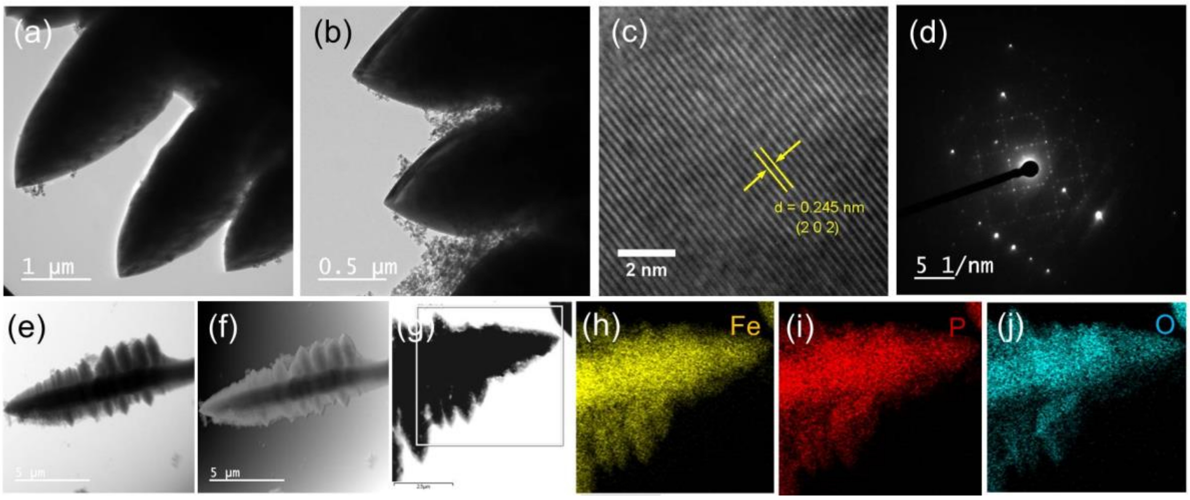

Figure S5. (a-b) TEM (c) HRTEM with d spacing corresponding to [2 0 2] plane (d) SAED (e-j) STEM and Elemental mapping of C0F10**.**

The branches with sharp edges developed from the stem of the dendrites can very well be observed for C0F10, especially in the high-angle annular darkfield scanning transmission electron microscopy (HAADF-STEM) image. The elemental mapping suggests the homogeneous distribution of all elements throughout the dendritic structure.

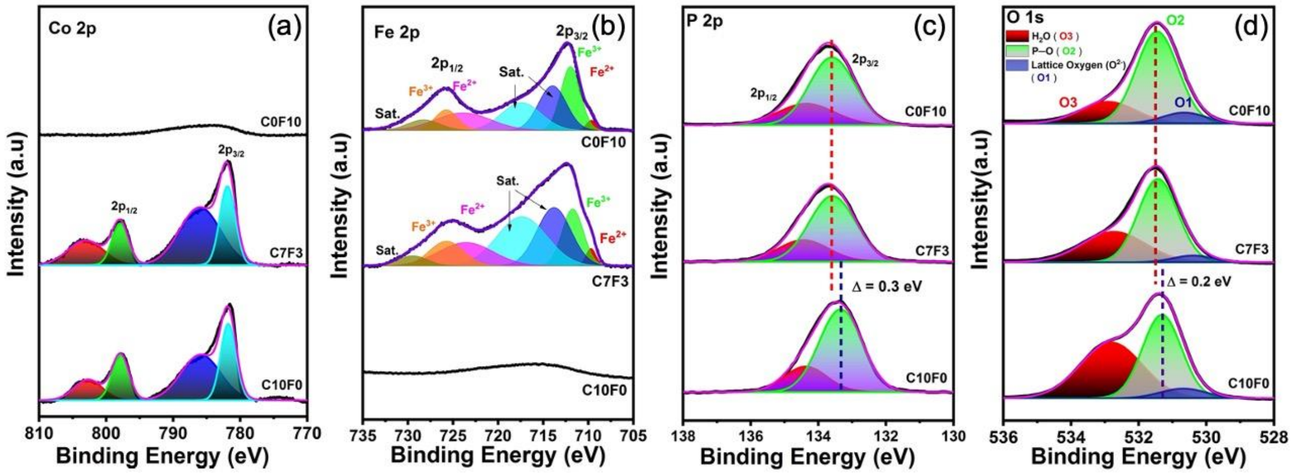

Figure S6. High-resolution XPS spectra of (a) Co 2p (b) Fe 2p (c) P 2p (d) O1s for C10F0, C7F3 and C0F10 samples.

The high-resolution spectra of Co 2*p* for C10F0 and C7F3 in Figure S6(a) shows the presence of two major peaks at 781.7 eV and 797.7 eV along with their satellite peaks at 786.1 eV and 803 eV for Co $2p_{3/2}$ and Co $2p_{1/2}$, respectively.[S4, S5] The binding energy difference of 16.03 eV between the primary peaks for Co $2p_{1/2}$ and Co $2p_{3/2}$ indicates the presence of typical Co^{2+} species.[S6] Similarly, the high-resolution spectra of Fe 2*p* for C7F3 and C0F10 show two prominent peaks at 711.8 eV and 725.4 eV for Fe $2p_{3/2}$ and Fe $2p_{1/2}$, which can be deconvoluted further indicating the presence of Fe^{2+} as well as Fe^{3+} in both cases along with two respective satellite peaks, as shown in Fig. S6(b).[S7] For obvious reasons, the flat Co 2*p* and Fe 2*p* were observed in case of C0F10 and C10F0, respectively. The core level P 2*p* spectra for all samples showed two distinct peaks (Fig. S6(c)) at binding energies 133.3 eV assigned for P $2p_{3/2}$ and 134.3 eV for P $2p_{1/2}$.[S8] Interestingly, a positive shifting by 0.3 eV can be observed for Fe-containing phosphates, i.e., in C7F3 and C0F10. Furthermore, in Fig. S6(d), the O 1*s* spectra deconvoluted into three peaks at 530.6 (O1), 531.5 (O2) and 533 eV (O3) corresponding to lattice oxygen (O^{2-}), P—O bond characteristic to the phosphate group and bound water of hydration respectively, observed in all the three samples of C10F0, C7F3 and C0F10. However, similar to P 2p, the O 1s also encounters a positive shifting by 0.2 eV in Fe-containing phosphates (C7F3 and C0F10) compared to no-

Fe phosphate (C10F0). Such an observation indicates a fruitful electronic interaction between Fe–P/O rather between Co–P/O, which may facilitate the OER activity making C7F3 as an active electrocatalyst. It is noteworthy to mention here the fact that C0F10 has also exhibited as the 2nd best electrocatalyst after C7F3, as the electronic interaction between Fe–P/O play a crucial role towards high OER activity.

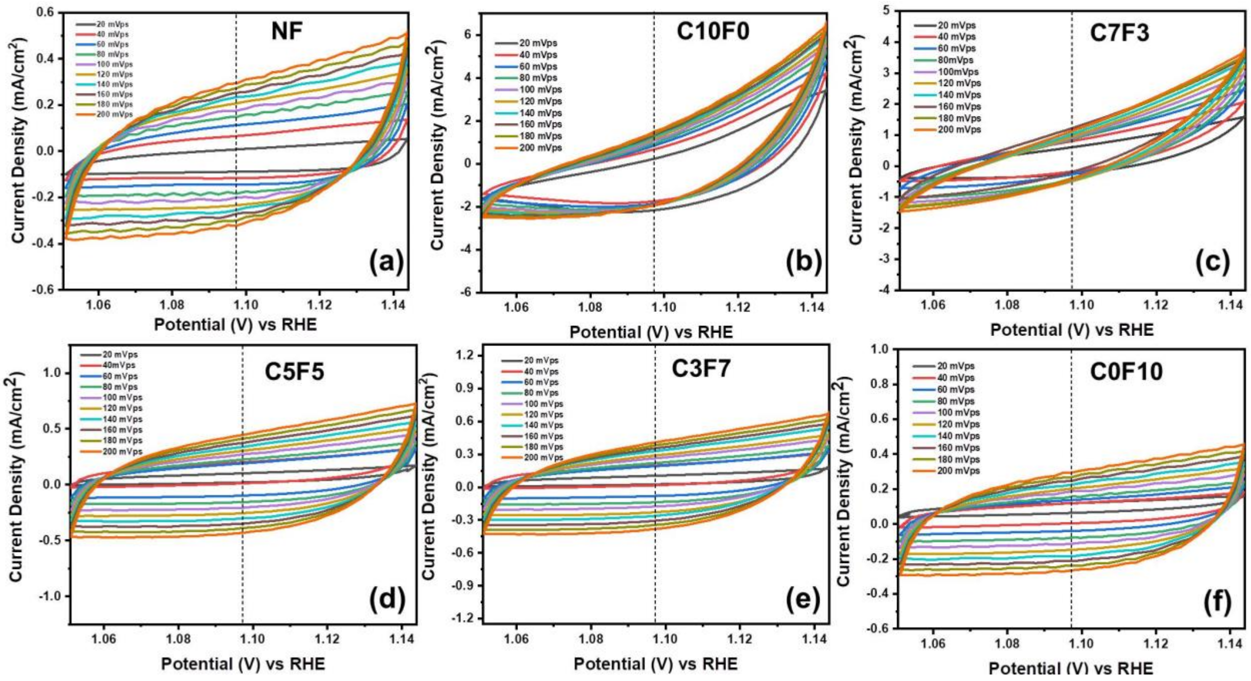

Figure S7. Cyclic voltammograms of (a) Bare NF (b) C10F0 (c)C7F3 (d) C5F5 (e) C3F7 and (f) C0F10 with a potential window from 1.05 to 1.14 V at different scan rates of 20, 40, 60, 80, 100, 120, 140, 160, 180, 200 mV sec^{-1} in 1.0 M KOH.

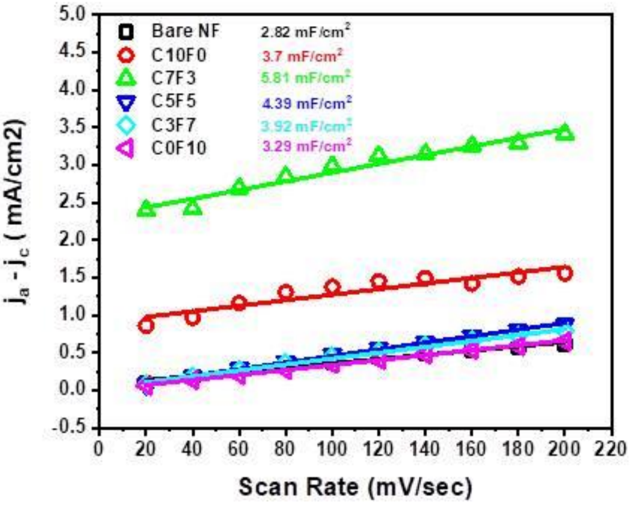

Figure S8. Plots of difference between anodic and cathodic current densities at different scan rates for all the catalysts to determine C_{dl} for OER.

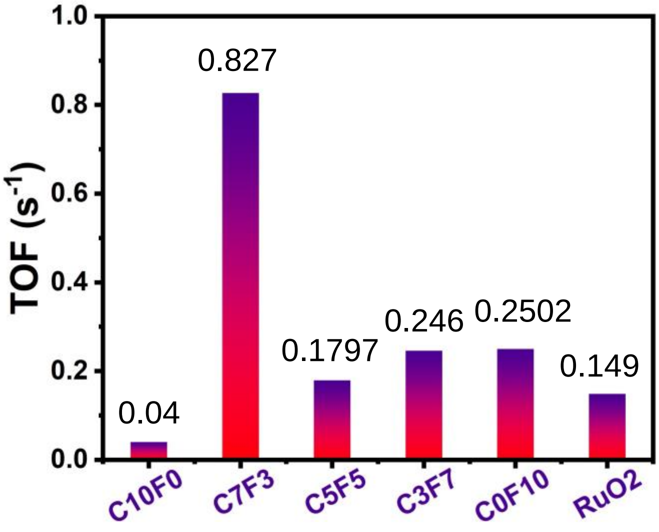

Figure S9: Turn over frequency (TOF) values determined at 280 mV overpotential for different electrocatalysts.

Turnover frequency (TOF) is considered to be a better activity marker for electrocatalysts to identify their inherent catalytic property. The TOF calculated at 280 mV overpotential for all electrocatalysts indicates almost three fold enhancement in activity for C7F3 compared to C0F10. The TOF values, as depicted in Figure S9, shows the inherent activities of electrocatalysts in line with the hypothesis proposed based on crystal structure.

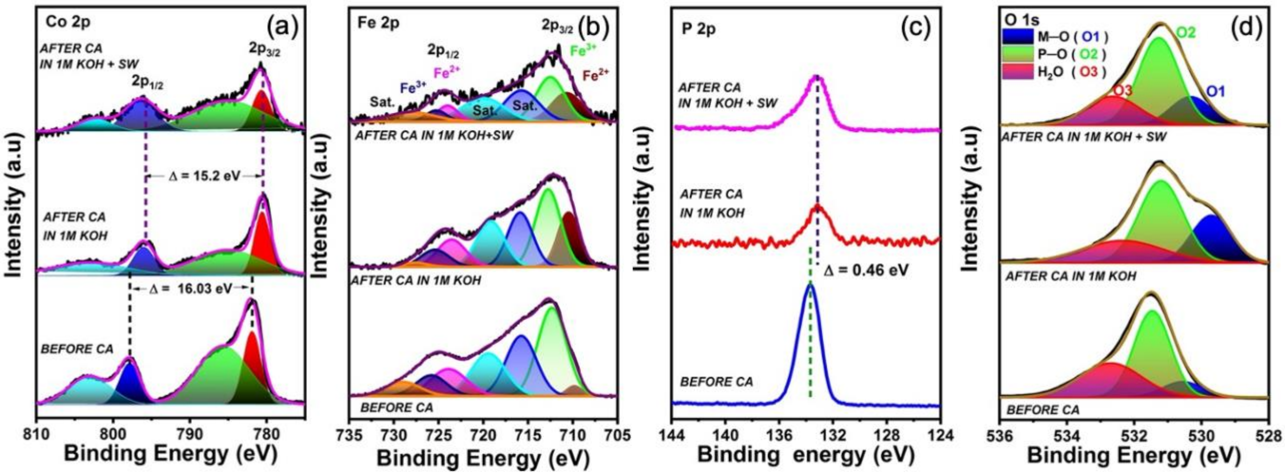

Figure S10. XPS analysis before and after stability test in 1M KOH and 1M KOH + Seawater electrolytes for (a) Co 2p (b) Fe 2p (c) P 2p and (d) O 1s in C7F3 sample.

The post OER characterization of C7F3 sample in 1M KOH as well as 1M KOH + Seawater have been carried out by XPS analysis. The careful examination of XPS data reveals no noticeable change in Fe 2*p* spectrum before and after stability test but interestingly changes in Co 2*p*, P 2*p* and O 1*s* can be noticed in both cases. After prolonged chronoamperometry test, the characteristic binding energy difference of 16.03 eV between the primary peaks for Co $2p_{1/2}$ and Co $2p_{3/2}$ changed to 15.2 eV indicating possible oxidation from Co^{2+} to Co^{3+} species in both electrolytes (Fig. S10(a)).[S6] In P 2*p* spectrum, the considerable weakening of P─O peak can be observed in both cases compared to pre-OER analysis indicating the possible change of the phosphate group in the material due to the electrochemical oxidation (Fig. S10(c)). Moreover, a significant change in the peak intensities of the deconvoluted peaks in O 1*s* spectrum can also be noticed after stability tests. A considerable increase in the peak intensity of O1 at 529.8 eV corresponding to M─O bond accompanied by significant decrease in O2 peak corresponding to P─O bond can be observed (Figure S10(d)). The observation can be attributed to the surface reconstruction phenomena involving the partial transition of phosphates into oxides or oxyhydroxides, often observed in metal phosphates and phosphides.[S9-S12]

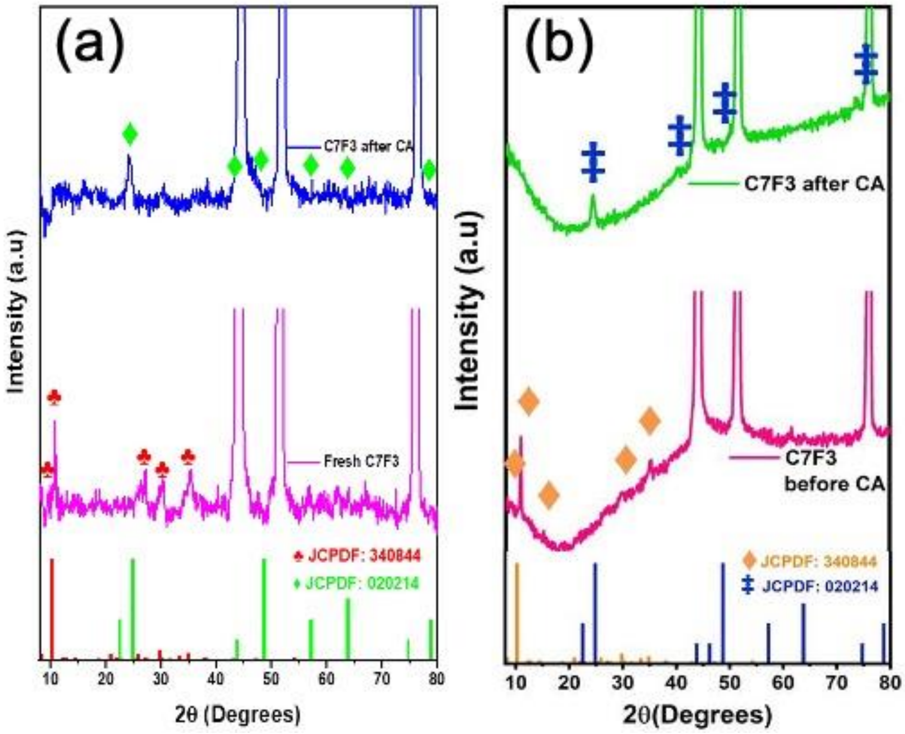

Figure S11. XRD pattern of the C7F3/NF electrode before and after stability test in (a) 1M KOH and (b) 1M KOH + Seawater.

XRD analysis of C7F3 on NF before and after CA tests in 1M KOH as well as 1M KOH + Seawater have also been performed. A clear evidence of transformation of cobalt phosphate hydrate (JCPDF No. 34-0844) into cobalt oxy-hydroxide (JCPDF No. 02-0214) post OER in both cases due to surface reconstruction can be observed, as shown in Figure S11.

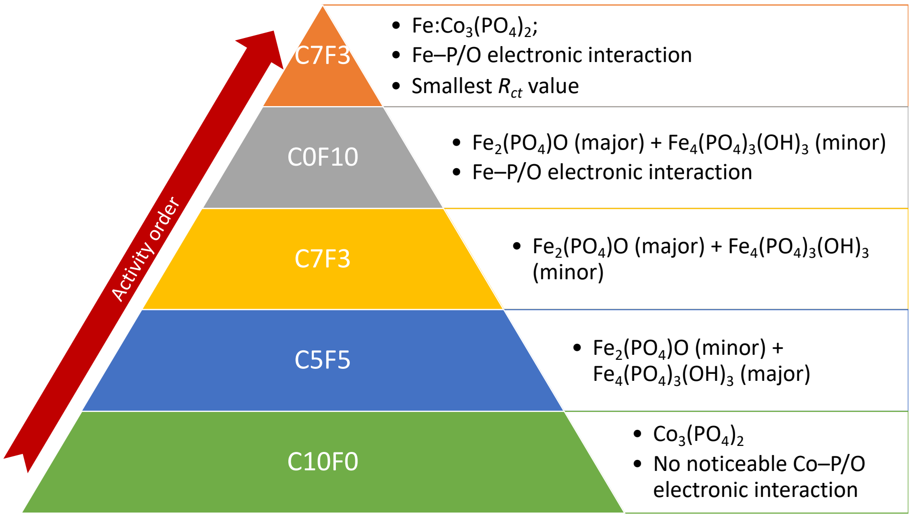

Figure S12: Activity pyramid and whereabouts.

Table S2. Comparison table of OER performance of various phosphates as electrocatalyst in alkaline freshwater electrolyte media.

Materials	**Electrolyte**	**Overpotential (η) (mV)**		**Tafel Slope (mV/dec)**	**Durability (h)**	**Ref.**
		η_{10}	**η_{100}**			
CoPi	1.0 M KOH	380	_	58.7	2	S13
CoPi-HSNPC-800	1.0 M KOH	320	410	85	20	S14
$Co_3(PO_4)_2$@N-C	1.0 M KOH	317	470 ($\eta_{87.1}$)	62	8	S15
CL-$Co_2P_2O_7$@C	0.1 M KOH	397	662 ($\eta_{155.7}$)	70	20.8	S16
$Co_3(PO_4)_2 \cdot 8H_2O$	1.0 M KOH	292	_	98	10	S17
H3LCoCN-NF	1.0 M KOH	215	_	61	12	S18
$Na_2Co_{0.75}Fe_{0.25}P_2O_7$/C	0.1 M KOH	300	_	47	100	S19
Cobalt phosphate NPs	1.0 M KOH	299	432	44	12	S20
$Co_3(OH)_2(HPO_4)_2$/NF	1.0 M KOH	240	320	69	56	S21
$(Co_{0.5}Ni_{0.5})_3(PO_4)_2$/Ni	1.0 M KOH	273	_	59.3	30	S22
$FePO_4$	1.0 M KOH	218	_	42.72	15	S23
FeP-FePxOy	1.0 M KOH	280	_	48	42	S24
CoFePi	0.1 M KOH	315	_	33	10	S25
NiCoFe phosphate	1.0 M KOH	240	_	58	24	S26
0.4Co:FePi	1.0 M KOH	266	_	42.6	10	S27

FCP-15	1.0 M KOH	273	298 (η_{50})	35.9	16	S28
Fe-doped Ni phosphate	1.0 M KOH	220	290 (η_{500})	37	10	S29
$Fe_3Co(PO_4)_4$@rGO	1.0 M KOH	_	237	57	70	S30
Am Fe-$Co_3(PO_4)_2$	1.0 M KOH	245	294	42	16	S31
$Fe_{2.95}(PO_4)_2(OH)_2$	1.0 M KOH	281	420 (η_{125})	46.48	12	S32
$Ni_2P_2O_7.8H_2O$	1.0 M KOH	239	_	51.5	9	S33
NiCo-2.0-800HP	1.0 M KOH	320		84	15	S34
$Mn_{1.5}Co_{1.5}(PO_4)_2$	1.0 M KOH	254	310	36	_	S35
Fe-$Co_3(PO_4)_2.4H_2O$	**1.0 M KOH**	**250**	**287**	**35.37**	**97**	**This work**

Table S3: Comparison table of OER performance of various Phosphorous-based catalysts in realistic alkaline sea water and various simulated sea water.

Materials	**Electrolyte**	**Overpotential (η) (mV)**		**Durability (h)**	**Ref.**
		η_{10}	**η_{100}**		
$NH_4CoPO_4 \cdot H_2O$	1 M KOH + 0.5 M NaCl	252	268	20	S36
Carbon-Coated $Na_2Co_{1-x}Fe_xP_2O_7$	0.5 M NaCl + 0.1 M KOH	285	1.6 V	100	S19
	1 M KOH + Seawater	325	_	50	
$Co\text{-}Fe_2P$	1 M KOH + 0.5 M NaCl	_	266	22	S37
NiFeP	1 M KOH + 1 M NaCl + 0.01 M $NaHCO_3$	100	129	100	S38
$Ni_2P\text{-}Fe_2P/NF$	1 M KOH + Seawater	_	305	36 @ 100 mA/cm^2 24 @ 500 mA/cm^2	S39
CoPx@FeOOH	1 M KOH + Seawater	235	283	80	S40
Fe–$Co_3(PO_4)_2.4H_2O$	**1.0 M KOH + 1 M NaCl**	**239**	**274**	_	**This work**
	0.5 M KOH + 1 M NaCl	**235**	**275**	_	
	0.5 M KOH + 0.5 M NaCl	**230**	**272**	_	
	1 M KOH + Seawater	**254**	**290**	**50**	

References

S1. S. A. Khalate, S. A. Kadam, Y. R. Ma, S. S. Pujari and U. M. Patil, *J. Alloys Compd.*, 2021, **885**, 160914.

S2. F. Sakhaei, E. Salahi, M. E. Olya, and I. Mobasherpour, *Micro Nano Lett.*, 2017, **12**, 920.

S3. P. S. Beurmann and I. Geowissenschaften, *Phosphorus Res. Bull*, 2002, **13**, 209.

S4. G. Ai, H. Li, S. Liu, R. Mo and J. Zhong, *Adv. Funct. Mater.*, 2015, **25**, 5706.

S5. S. Zhang, B. Ni, H. Li, H. Lin, H. Zhu, H. Wang and X. Wang, *Chem. Commun.* 2017, **53**, 8010.

S6. R. Zhang, G. van Straaten, V. Di Palma, G. Zafeiropoulos, M. C. van de Sanden, W. M. Kessels, M. N. Tsampas and M. Creatore, *ACS Catal.*, 2021, **11**, 2774.

S7. Y. Huang, L. W. Jiang, B. Y. Shi, K. M. Ryan and J. J. Wang, *Adv. Sci.*, 2021, **8**, 2101775.

S8. R. Zhang, G. Straaten, V. Palma, G. Zafeiropoulos, M.C.M. Sanden, W.M.M. Kessels, M.N. Tsampas, M. Creatore, *ACS Catal*. 2021, **11**, 2774−2785.

S9. R. Guo, X. Lai, J. Huang, X. Du, Y. Yan, Y. Sun, G. Zou and J. Xiong, ChemElectroChem, 2018, **5**, 3822.

S10. J. Huang, Y. Sun, Y. Zhang, G. Zou, C. Yan, S. Cong, T. Lei, X. Dai, J. Guo, R. Lu and Y. Li, *Adv. Mater.*, 2018 , **30**, 1705045.

S11. N. L. W. Septiani, Y. V. Kaneti, K. B. Fathoni, K. Kani, A. E. Allah, B. Yuliarto, H. K. Nugraha, Dipojono, Z. A. Alothman, D. Golberg and Y. Yamauchi, *Chem. Mater.*, 2020, **32**, 7005.

S12. K. Xu, H. Cheng, L. Liu, H. Lv, X. Wu, C. Wu, Y. Xie, *Nano Lett.*, 2017, **17**, 578.

S13. M. Pramanik, C. Li, M. Imura, V. Malgras, Y. M. Kang and Y. Yamauchi, *Small*, **12**, 1709.

S14. L. Chen, J. T. Ren, Y. S. Wang, W. W. Tian, L. J. Gao, and Z. Y. Yuan, *ACS Sustain. Chem. Eng.*, 2019, **7**, 13559.

S15. C. Z. Yuan, Y. F. Jiang, Z. Wang, X. Xie, Z. K. Yang, A. B. Yousaf, A. W. Xu, *J. Mater. Chem. A*, 2016, **4**, 8155.

S16. Y. Chang, N. E. Shi, S. Zhao, D. Xu, C. Liu, Y. J. Tang, Z. Dai, Y. Q. Lan, M. Han, J. Bao, *ACS Appl. Mater. Interfaces*, 2016, **8**, 22534.

S17. P. K. Katkar, S. J. Marje, S. B. Kale, A. C. Lokhande, C. D. Lokhande and U. M. Patil, *CrystEngComm*, 2019, **21**, 884.

S18. T. Zhou, Y. Du, D. Wang, S. Yin, W. Tu, Z. Chen, A. Borgna, R. Xu, *ACS Catal.,* 2017, **7**, 6000.

S19. H. J. Song, H. Yoon, B. Ju, D. Y. Lee and D. W. Kim, *ACS Catal.*, 2020, **10**, 702.

S20. S. S. Sankar, A. Rathishkumar, K. Geetha and S. Kundu, *Energy Fuels*, 2020, **34**, 12891.

S21. P. W. Menezes, C. Panda, C. Walter, M. Schwarze and M. Driess, *Adv. Funct. Mater.*, 2019, **29**, 1808632.

S22. J. Li, W. Xu, D. Zhou, J. Luo, D. Zhang, P. Xu, L. Wei, D. Yuan, *J. Mater. Sci.,* 2018, **53**, 2077.

S23. L. Yang, Z. Guo, J. Huang, Y. Xi, R. Gao, G. Su, W. Wang, L. Cao, B. Dong, *Adv. Mater.*, 2017, **29**, 1704574.

S24. J. Xu, D. Xiong, I. Amorim and L. Liu, *ACS Appl. Nano Mater.*, 2018, **1**, 617.

S25. Y. Zhou and H. C. Zeng, *Small*, 2018, **14**, 1801882.

S26. M. A. Z. G. Sial, H. Lin and X. Wang, *Nanoscale*, 2018, **10**, 12975.

S27. Z. Wang, M. Liu, J. Du, Y. Lin, S. Wei, X. Lu, J. Zhang, *Electrochim. Acta*, 2018, **264**, 244.

S28. Y. Li and C. Zhao, *Chem. Mater.*, 2016, **28**, 5659.

S29. S. Sultan, M. Ha, D. Y. Kim, J. N. Tiwari, C. W. Myung, A. Meena, T. J. Shin, K. H. Chae, K. S. Kim, *Nat. Commun.*, 2019, **10**, 1.

S30. J. Zhang, X. Tan, W. Wang, L. Cao and B. Dong, *Sustain. Energy Fuels*, 2020, **4**, 4704.

S31. S. A. Khalate, S. A. Kadam, Y. R. Ma, S. S. Pujari, S. J. Marje, P.K. Katkar, A. C. Lokhande and U. M. Patil, *Electrochim. Acta* , 2019, **319**, 118.

S32. S. J. Marje, P. K. Katkar, S. B. Kale, A. C. Lokhande, C. D. Lokhande and U. M. Patil, *J. Alloys Compd.*, 2019, **779**, 49.

S33. N. L. W. Septiani, Y. V. Kaneti, K. B. Fathoni, Y. Guo, Y. Ide, B. Yuliarto, X. Jiang, H. K. Dipojono, D. Golberg, Y. Yamauchi, *J. Mater. Chem. A*, 2020, **8**, 3035.

S34. D. Chinnadurai, R. Rajendiran, O. L. Li and K. Prabakar, *Appl. Catal. B Environ.*, 2021, **292**, 120202.

S35. Z. Song, K. Wang, Q. Sun, L. Zhang, J. Li, D. Li, P. W. Sze, Y. Liang, X. Sun, X. Z. Fu, J. L. Luo, *Adv. Sci.*, 2021, **8**, 2100498.

S36. S. Wang, P. Yang, X. Sun, H. Xing, J. Hu, P. Chen, Z. Cui, W. Zhu, Z. Ma, *Appl. Catal. B Environ.*,2021, **297**, 120386.

S37. J. Liu, X. Liu, H. Shi, J. Luo, L. Wang, J. Liang, S. Li, L. M. Yang, T. Wang, Y. Huang and Q. Li, *Appl. Catal. B Environ.*, 2022, **302**, 120862.

S38. L. Wu, L. Yu, F. Zhang, B. McElhenny, D. Luo, A. Karim, S. Chen and Z. Ren, *Adv. Funct. Mater.*, 2021 , **31**, 2006484.

S39. L. Wu, L. Yu, L. B. McElhenny, X. Xing, D. Luo, F. Zhang, J. Bao, S. Chen, Z. Ren, *Appl. Catal. B Environ.*, 2021, **294**, 120256.